Seismicity modulation due to hydrological loading in a stable continental region: a case study from the Jektvik swarm sequence in Northern Norway

Hasbi Ash Shiddiqi[1*]), Lars Ottemöller[1], Stéphane Rondenay[1], Susana Custódio[2], Vineet K. Gahalaut[3], Rajeev K. Yadav[3], Felix Halpaap[1], and Kalpna Gahalaut[3]

[1] *Department of Earth Science, University of Bergen, Bergen, Norway.*

[2] *Instituto Dom Luiz, Faculdade de Ciências, Universidade de Lisboa, Lisboa, Portugal.*

[3] *CSIR-National Geophysical Research Institute, Hyderabad, India.*

[*]) *corresponding author: hasbi.shiddiqi@uib.no*

manuscript submitted to Geophysical Journal International

SUMMARY

Seismic swarms have been observed for more than 40 years along the coast of Nordland, Northern Norway. However, the detailed spatio-temporal evolution and mechanisms of these swarms have not yet been resolved due to the historically sparse seismic station coverage. An increased number of seismic stations now allows us to study a nearly decade-long swarm sequence in the Jektvik area during the 2013-2021 time window. Our analysis resolves four major groups of events, each consisting of several spatial clusters, that have distinct spatial and temporal patterns. Computed focal mechanism solutions are predominantly normal with NNE-SSW strike direction reflecting a near-vertical maximum principal stress and a NW-SE near-horizontal minimum principal stress, which are controlled by local NW-SE extension. We attribute the swarm sequence to fluid-saturated fracture zones that are reactivated due to this local extension. Over the time period, the activity tends to increase between February and May, which coincides with the late winter and beginning of spring time in Norway. We hypothesize

that the seismicity is modulated seasonally by hydrological loading from snow accumulation. This transient hydrological load results in elastic deformation that is observed at local GNSS stations. The loading is shown to promote failure in a critically stressed normal faulting system. Once a segment is activated, it can then also trigger neighboring segments via stress transfer. Our new results point to a close link between lithosphere and hydrosphere contributing to the occurrence of seismic swarm activity in northern Norway.

Key words: Seismicity and tectonics; Continental tectonics: extensional; Arctic region

1 INTRODUCTION

The coastal region of Nordland, northern Norway, experiences considerable earthquake swarm activity. The swarms are situated within one of the most seismically active regions in mainland Norway, where more than 200 earthquakes above M_L 0.5 are recorded annually, and which also hosted one of the largest documented earthquakes in Fennoscandia: the 1819 M 5.9 Lurøy earthquake (Muir-Wood, 1989; Bungum & Olesen, 2005; Mäntyniemi et al., 2020) (Fig. 1.a). Many spatio-temporal earthquake clusters have been reported here over the past few decades, including those of Meløy in 1978-1979 (Bungum et al., 1979, 1982), Steigen in 1992 (Atakan et al., 1994), Rana in 1998-1999 and 2005 (Hicks et al., 2000; Gibbons et al., 2007) and Jektvik in 2015-2016 (Michálek et al., 2018). Although some hypotheses to explain the regional seismicity in Nordland have been proposed, a detailed characterisation of these swarms has not been possible until now due to the sparsity of seismic stations. Addressing this shortcoming is important as swarms have the potential to help us better understand deformation in the region and the physical properties of the crust. These results can then be utilised to refine seismic hazard assessment in an intraplate region that experiences both swarms and large earthquakes.

The Nordland region has been shaped by a series of major geological episodes. The collision between Baltica and Laurentia resulted in the Caledonian orogeny with high mountains. It was followed by orogenic collapse in the Devonian and then rifting during the opening of the North Atlantic Ocean. Nordland is part of the Caledonian domain, which is dominated by nappe complexes as a result of the collision (Corfu et al., 2014). The area is mostly covered by the Upper and

Uppermost Allochthons, which were thrust onto the Precambrian basement (Roberts, 1988; Corfu et al., 2014)). Following the collapse of the Caledonides, extensional shear zones and detachment faults were formed (Fossen, 2010). Part of the Jektvik area, which is the focus in this study, consists of Precambrian granitoids dominated by granitic and tonalite gneiss (Fig. 1.b). The dominant strikes of extensional faults and shear zones in the area are NNE-SSW and WNW-ESE (Fig. 1.b). This is supported by detailed mapping of the Jektvik region, which identified a small shear zone and a set of fractures with dominant NNE-SSW and WNW-ESE directions (Rostad, H., 1990).

Earthquake fault plane solutions and observations of deformation indicate a rather complex stress regime in Nordland and the adjacent offshore areas. While the mechanisms of earthquake located along the shelf edge are mainly characterised by thrust faulting, those of earthquakes located along the coast are dominated by normal faulting (Michálek et al., 2018; Janutyte et al., 2017; Shiddiqi et al., 2022). The normal faulting events along the coast reflect a deviation from the compressive regional stress, which possibly arises due the additional interference from Glacial Isostatic Adjustment (GIA) and sediment redistribution (e.g., Bungum et al., 2010; Gradmann et al., 2018). Nordland is rising due to GIA, with an average uplift rate of around 4 mm/year in the coastal area (Kierulf et al., 2014). Furthermore, the differences between Global Navigation Satellite System (GNSS) observations and GIA models in Nordland are larger than in other parts of Scandinavia, which may indicate strong subsurface lateral heterogeneity or neotectonic processes (Kierulf et al., 2014; Kierulf, 2017).

Intraplate seismic swarms in various stable continental regions (SCR) worldwide can offer clues as to what causes swarms in Nordland. Swarms are often attributed to the reactivation of pre-existing faults under regional and local stress conditions (e.g., Talwani, 2017). Fluids can play an important role in facilitating seismic swarms by reducing the normal stresses via pore-pressure increase. In addition, hydrological load changes from water bodies, soil moisture and snow cause elastic deformation, which often is observable in GNSS data (e.g., Drouin et al., 2016; Springer et al., 2019). The load change can be significant enough to modulate stresses, pore-pressure and eventually seismic rupture, as suggested by Hainzl et al. (2006); Craig et al. (2017); Gahalaut et al. (2022). Possible links between hydrological processes and swarms have been inferred in various

intraplate regions, notably Mt. Hochstaufen in Germany (Hainzl et al., 2006), New Madrid in the USA (Bisrat et al., 2012), and Palghar in Western India (Sharma et al., 2020; Gahalaut et al., 2022). In order to investigate the possible role of hydrological processes in Nordland, we first need to characterize precisely the spatio-temporal evolution of seismicity - something that has not been possible until now.

In this study, we take advantage of improved station coverage to investigate the spatio-temporal distribution of the swarm sequence in Jektvik, which has been active for more than nine years. Our objective is to develop a high resolution earthquake catalog, supplemented with computations of focal mechanisms. We improve the existing earthquake catalog by adding previously undetected events using a deep-learning based algorithm. Then we relocate the earthquakes and identify clusters using differential times and waveform similarity. Using the high-quality seismicity and computed focal mechanisms solutions, we image the fault systems corresponding to the regions where the swarms occurred. We finally use these results to investigate the possible processes that can trigger the swarm sequence and the mechanisms that cause seismicity to migrate within and between fault segments.

2 IMPROVING THE EARTHQUAKE CATALOG

To date, swarm activity in Nordland has been characterized mainly using relatively sparse permanent stations, which usually results in catalogs with magnitude of completeness ≥ 1.0. This is clearly insufficient to investigate the processes responsible for swarm activity. To address this shortcoming, we developed a high-quality earthquake catalog for Nordland by combining data from permanent stations with those from temporary stations deployed in the region over the past decade. Using this new expanded dataset, we first performed automatic event detection and phase picking to process events that have not been reported in the Norwegian National Seismic Network (NNSN) catalog (Ottemöller et al., 2018). Then we performed manual phase checking, hypocenter location and local magnitude determination using SEISAN software package (Havskov & Ottemoller, 1999; Havskov et al., 2020).

To establish a comprehensive dataset, we collected and integrated relevant catalogs and wave-

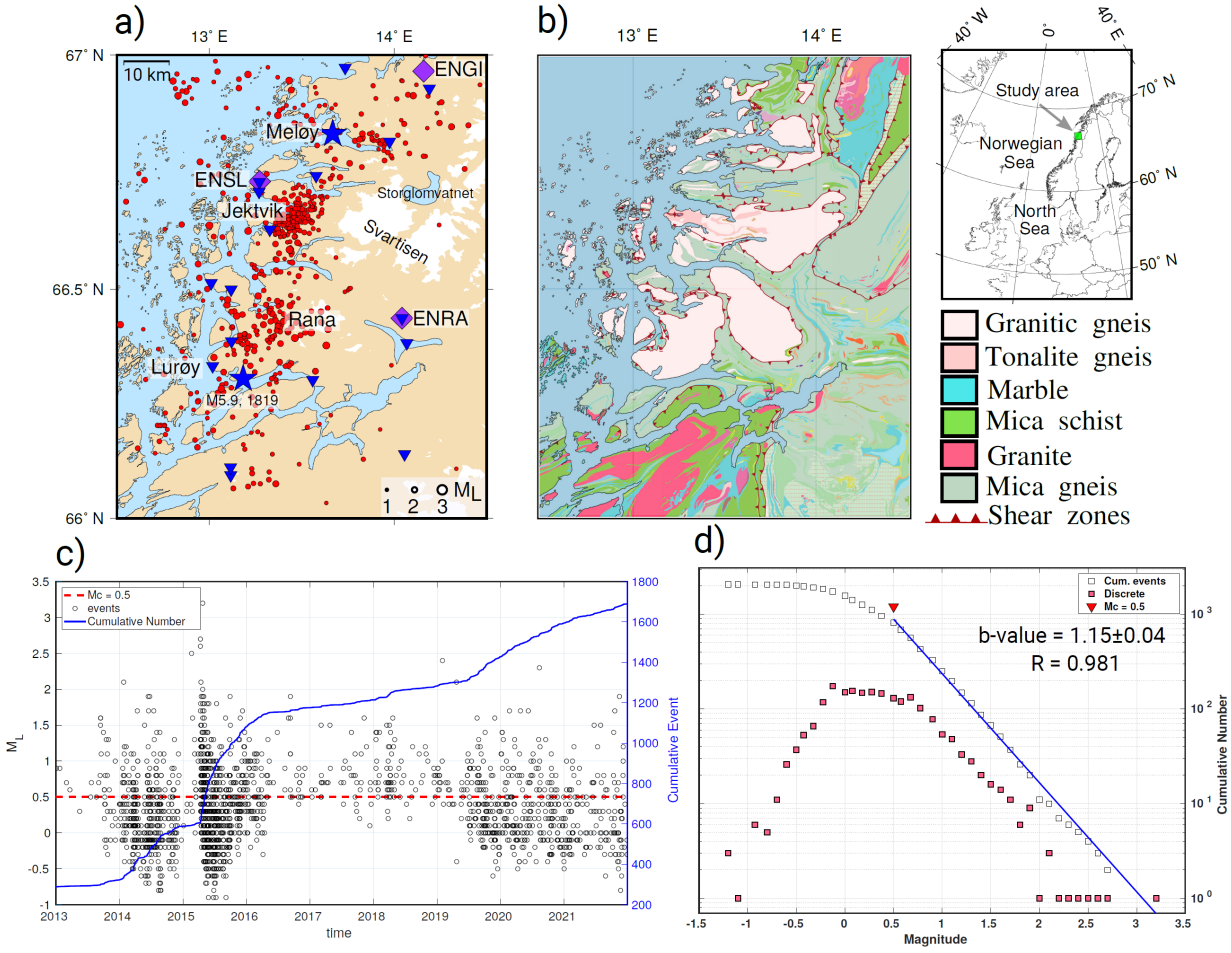

Figure 1. a) Seismicity maps ($M_L \geq$ 1.0) in Jektvik and nearby regions. Epicenters are shown as red circles. Notable previous seismic events are marked as blue stars: the estimated location of the M 5.9 1819 Lurøy earthquake, and the center of the 1978-1979 Meløy swarms. Seismic and GNSS stations (ENSL, ENGI and ENRA) used in this study are depicted as blue inverted triangles and purple diamonds, respectively. Storglomvt: Storglomvatnet water reservoir. b) Bedrock geology map for the area from the National Bedrock Database from Geological Survey of Norway (2011). Inset map shows the location of the study area in a larger geographical context. c) Temporal variation of earthquakes with M_L and cumulative number of earthquakes. The magnitude of completeness (Mc = 0.5) is shown as dashed red line. d) Frequency magnitude distribution of the catalog. The b-value for the whole dataset is 1.15.

form data from temporary and permanent seismic stations. As a starting database, we used the NNSN earthquake catalog in the 2013-2021 time window (with a cutoff year set at 2013 because station coverage was too sparse prior to that). The number of stations in the region has grown significantly since 2013 owing to the deployment of two temporary networks: Neonor2, 2013-2016 (Michálek et al., 2018) and Scanlips3D, 2013-2014 (England et al., 2016). Since 2018, the NNSN

has added six permanent stations in Nordland within 150 km of Jektvik. These changes have resulted in a variable station coverage over time that can be appraised by compiling the monthly number of stations operating within 150 km from the study area over the 2013-2021 period (see Fig. S1). The number of stations reached a maximum of 36 in 2014 and a minimum of 4 between June 2016 and October 2018, which resulted in a slightly decreased detection capability during this latter time window. It will be important to be aware of these fluctuations when we assess the magnitude of completeness of the whole catalog.

The integration of the various data sets allowed us to expand the existing catalogue (a product of routine processing by the NNSN) by adding smaller earthquakes. This was done by utilizing the Eqtransformer Python package (Mousavi et al., 2020) - a powerful deep-learning based tool employed for event detection and phase picking. The picker is trained using the STanford EArthquake Dataset (STEAD) (Mousavi et al., 2019), consisting of a global earthquake database that includes data from a few Norwegian earthquakes. Despite the fact that the picker was trained using mostly data from other regions, previous studies have shown that it can perform well under such conditions (e.g., Mousavi et al., 2020; Jiang et al., 2022; Münchmeyer et al., 2022). An example of event detection and phase picking for events with M_L 0.4 and M_L -0.8, recorded by the station closest to the Jektvik swarm (N2VG), is shown in Fig. S2. For each event detected and processed by Eqtransformer, we used SEISAN to perform a manual check of recordings from all available stations and to pick phase arrivals that may have been missed by the routine automated workflow. After verification, the newly detected events were merged with the NNSN catalog. We used events that were detected both by NNSN and Eqtransformer to evaluate the accuracy of the automatic picking results and estimate the picking errors for the whole catalog. Based on this comparison, we found that the mean difference between NNSN and Eqtransformer phase picks is 0.12 s for P-waves and 0.14 s for S-waves (Fig. S3) and conclude that manual and Eqtransformer processing are compatible. This is essential for further processing and interpretation of the combined catalog.

For the set of detected events we initially determined hypocenter locations by travel-time inversion using the Hypocenter program (Lienert & Havskov, 1995). The program requires a velocity model to compute travel-times - we used the minimum 1-D velocity model developed for the

Nordland region by Shiddiqi et al. (2022). We estimated the location errors using a bootstrap re-sampling analysis similar to that of Shiddiqi et al. (2019), in which the inversion procedure was repeated 100 times by adding random Gaussian noise with a standard error of 0.2 s to the arrival times and recomputing the hypocenter locations. Error estimates were then computed by taking the standard deviation of the 100 realizations in the horizontal (σ_H) and vertical directions (σ_V). In order to get reliable hypocenters without discarding large number of earthquakes, the events retained for further processing and interpretation are chosen based on a set of somewhat relaxed selection criteria: 1) a minimum of five picks with at least two S-picks, 2) azimuthal gap $\leq$ 225°, and 3) both σ_H and $\sigma_V \leq$ 5.0 km. A total of 2063 events fit these criteria - including 1095 newly detected earthquakes. The histograms of σ_H and σ_V are shown in Fig. 2, and the mean of σ_H and σ_V are 1.14 km and 1.57 km, respectively.

We measured earthquake size for all detected earthquakes by computing local magnitudes, M_L, using the scale for Norway (Alsaker et al., 1991). This is achieved by measuring the maximum amplitudes of Sg waves on simulated Wood-Anderson traces of the vertical channels that are filtered between 2.0 - 18.0 Hz. We chose this frequency band because it yields considerably higher signal-to-noise ratio for small earthquakes compared to the standard frequency band of 1.25 - 18 Hz applied by the NNSN (see Havskov & Ottemöller (2010)). The amplitude measurements were performed automatically using the Automag program in SEISAN. To mitigate M_L overestimation at short-distance stations, we added a correction term for Northern Norway: $-0.74e^{0.09r}$, where r is distance in km (Luckett et al., 2018). With this correction, the M_L scale for Northern Norway becomes:

$$M_{\mathrm{L}} = log(amp) + 0.91log(r) + 0.00087r - 0.74e^{0.09r} - 1.67 \quad (1)$$

where amp is the amplitude on the Wood-Anderson seismogram in nanometers. The magnitude-frequency distribution of the improved catalog gives an overall b-value of 1.15 and a magnitude of completeness (M_c) of M_L 0.5 (Fig. 1.d).

We computed focal mechanisms for events after May 2016 to complement previous studies that had computed fault plane solutions for earthquakes between August 2013 - May 2016 in the Jektvik area (Michálek et al., 2018; Shiddiqi et al., 2022). We used first motion polarities picked

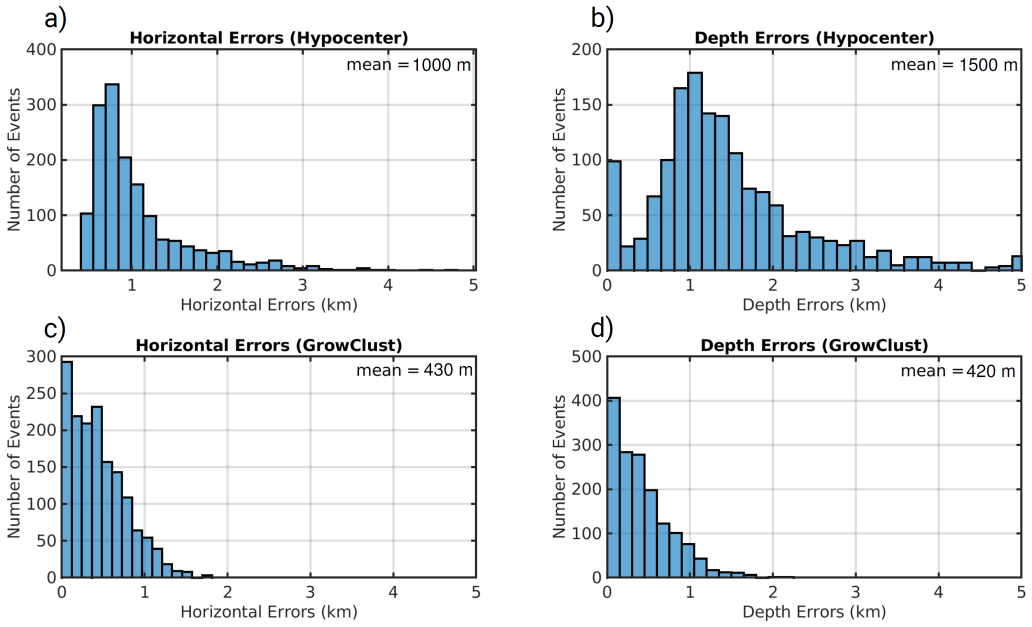

Figure 2. Comparison of initial and relative location errors estimated using a bootstrap resampling method. Histograms of σ_H and σ_V of initial locations shown in a) and b). Only earthquakes relocated by GrowClust program are presented here. Histograms of relative location σ_H and σ_V determined using GrowClust program are shown in c) and d).

on unfiltered vertical traces, as well as amplitudes of direct Pg and Sg waves from distances $\leq$100 km measured on the vertical and transverse traces, respectively. The Pg and Sg amplitudes were corrected for crustal attenuation and free surface. To correct for attenuation, we adopted the Q value for mainland Norway $Q_{Lg} = 529f^{0.42}$ (Demuth et al., 2019), and assumed that Q_P and Q_S have the same value. The focal mechanisms were estimated using the Focmec program (Snoke, 2003). Due to the relatively small number of stations, we set more relaxed acceptable solution criteria than Michálek et al. (2018); Shiddiqi et al. (2022). We did not allow for any polarity error, and the acceptable amplitude ratios were required to have a logarithmic misfit less than 0.2 (see the Focmec manual (Snoke, 2017)). Of the computed mechanisms, we retained those that satisfy the following criteria: 1) the input data include at least five polarities covering both compression and dilatation quadrants of the focal sphere, 2) more than half of the observations must yield acceptable amplitude ratios, and 3) all solutions obtained for one event have to be similar: P- and T-axes concentrate within $\sim \frac{1}{10}$ areas on the focal sphere.

3 HYPOCENTER RELOCATION AND CLUSTERING

To improve the locations of events and assess objectively their degree of clustering, we employed the GrowClust relocation program that combines earthquake relocation and hierarchical clustering (Trugman & Shearer, 2017). As input data, Growclust uses travel-time differences and waveform cross-correlation coefficients (CC) for event pairs recorded on single stations. We used the Obspy package (Beyreuther et al., 2010; Krischer et al., 2015; Megies et al., 2019) to carry out key pre-processing operations on the input waveforms, including instrument response removal and band-pass filtering between 3.0 to 9.0 Hz, and then the EQcorrscan package (Chamberlain et al., 2017) to compute the travel-time differences and waveform correlations. We computed correlations of event pairs with maximum separation of 10 km.

The Growclust algorithm employs a grid-search approach to minimize the L1 norm, which is least sensitive to outliers of travel-time residuals within a cluster. GrowClust uses a 1-D velocity model to compute the synthetic travel-times for direct arrivals (i.e., Pg and Sg), and does not take into account Moho refracted arrivals (i.e., Pn and Sn). Therefore, we selected observations from stations closer than the cross-over distance of 150 km in our case. Event clusters were identified using a hierarchical clustering algorithm in GrowClust, where events are paired based on a number of criteria: minimum CC cutoff (rmin), maximum root-mean-square of travel-time residuals (rms-max), and distance. We tested a number of rmin values to find the preferred value. The rmsmax was set to a value of 0.2 second, which was found to be suitable in previous studies (Trugman & Shearer, 2017; Ross et al., 2020). Relaxing the rmsmax value can increase the number of relocated events, but at the same time reduce the relative location quality. We allowed events to join a cluster if they are separated by no more than 8 km distance in the initial catalog, and 4 km distance in the relocated catalog. The relocation uncertainties (σ_H and σ_V) were estimated using bootstrap resampling method, which is integrated within the GrowClust algorithm. Furthermore, we evaluated clustering robustness by inspecting earthquake distribution and the hierarchical clustering trees (dendrogram), which show the links between events by means of CC and event clustering.

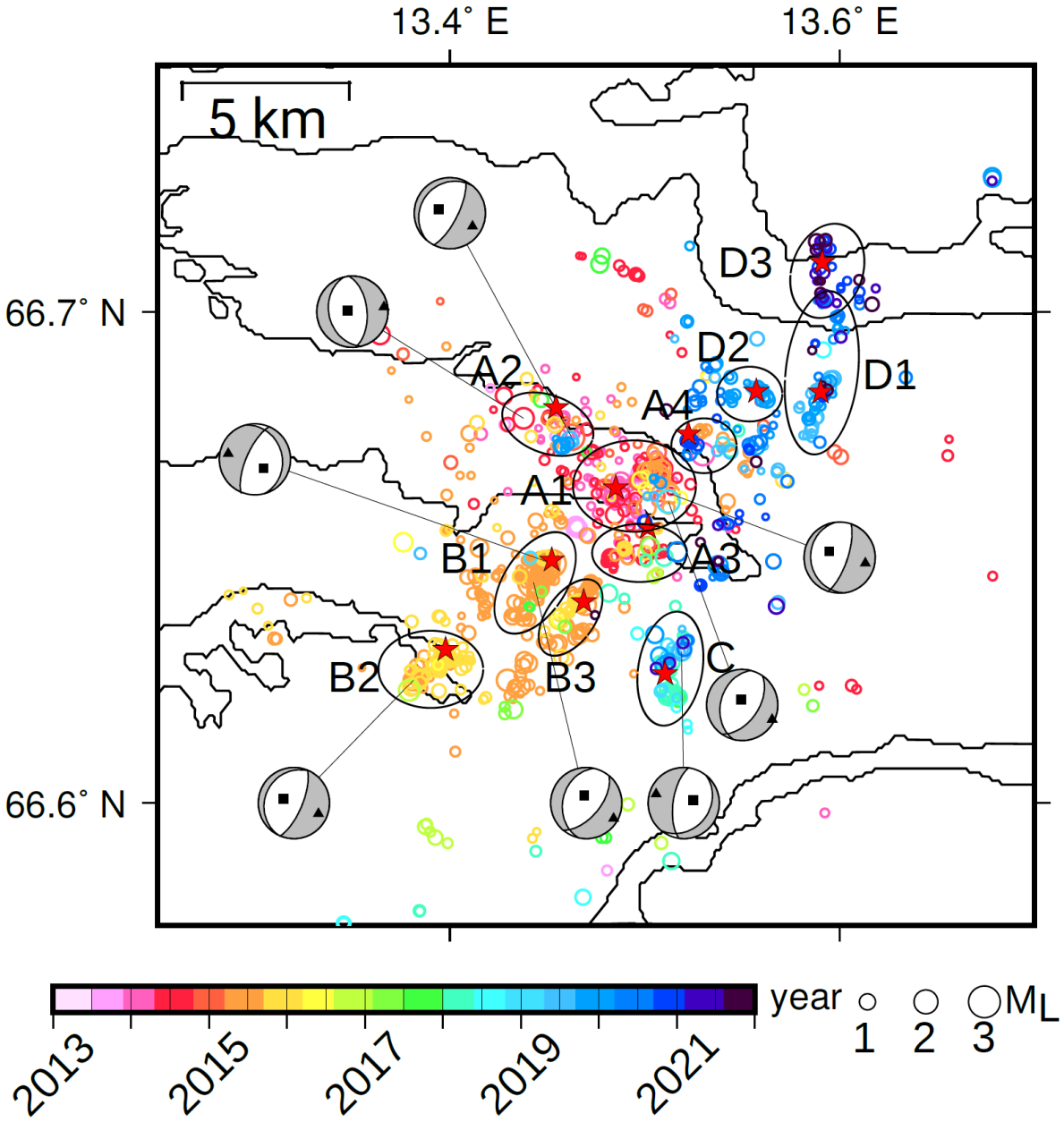

Figure 3. Relocated earthquakes ($M_L \geq 0$) and focal mechanism solutions in Jektvik for the period of 2013 to 2021. Epicenters are shown as open circle colored with time of occurrence. The major clusters that contain more than 25 events are marked with ellipses. The first event in each cluster is marked as red star. The P- and T-axes of the focal mechanisms are shown as black squares and triangles, respectively.

4 RESULTS

The analysis described in the previous sections yields an improved earthquake catalog that contains differential times, cross correlations, amplitudes and polarities. This provides us with more accurate relative locations, cluster identification, fault plane solutions and magnitude estimates.

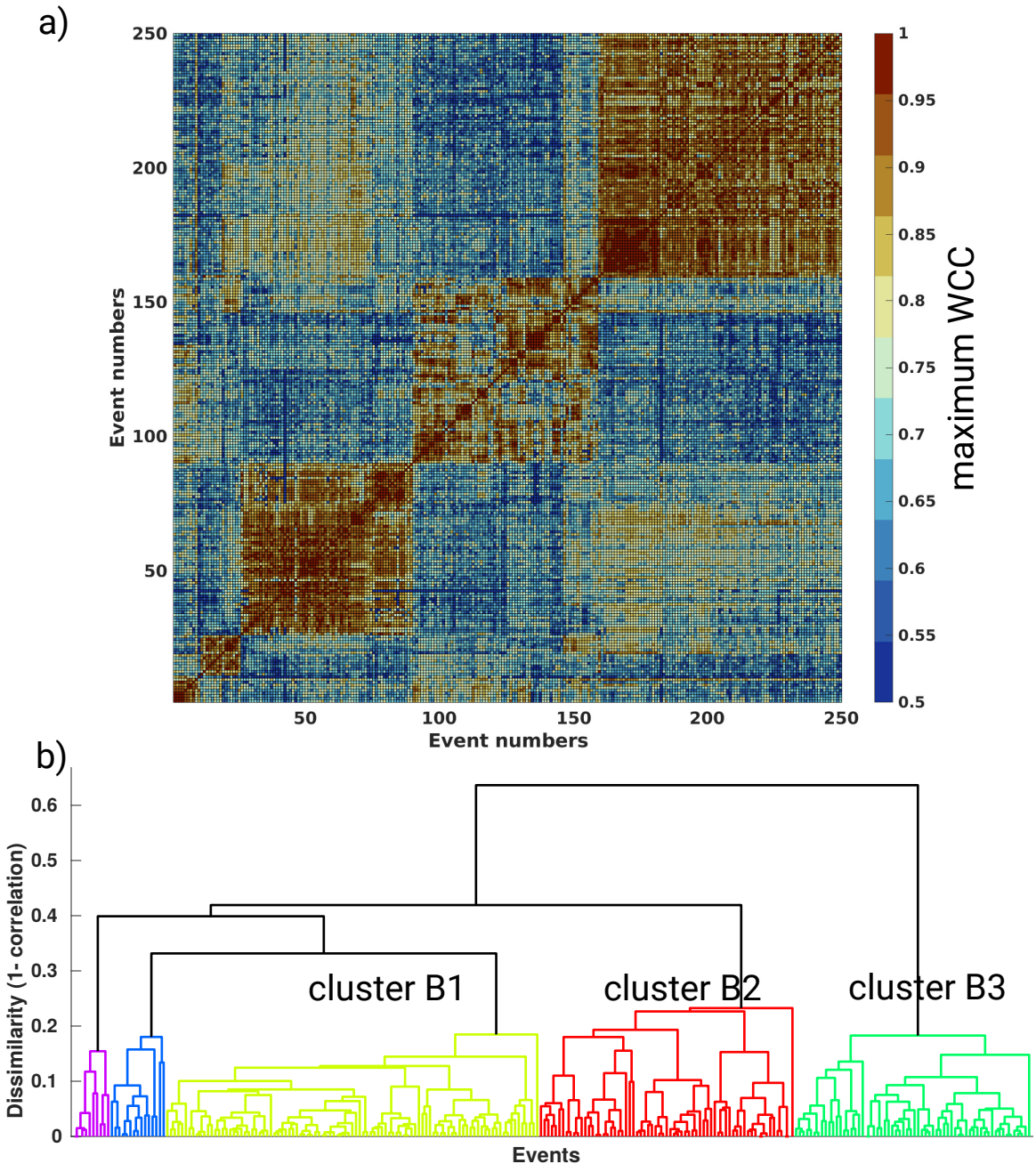

Figure 4. Waveform cross-correlation result and event links for events around group B. a) sorted CC matrix shows three majors clusters, b) dendrogram plot, which shows links between events by means of CC, also indicate that there are three majors clusters in Group B.

In total we relocated 1590 events. On average, each event location was determined by more than 200 differential times. The quality of the relative locations is best expressed via the reduction in location error compared to the initial hypocenters (Fig. 2). The average σ_H and σ_V of the relocated earthquakes are 430 and 420 meters, respectively, in comparison to 1000 and 1500 meters

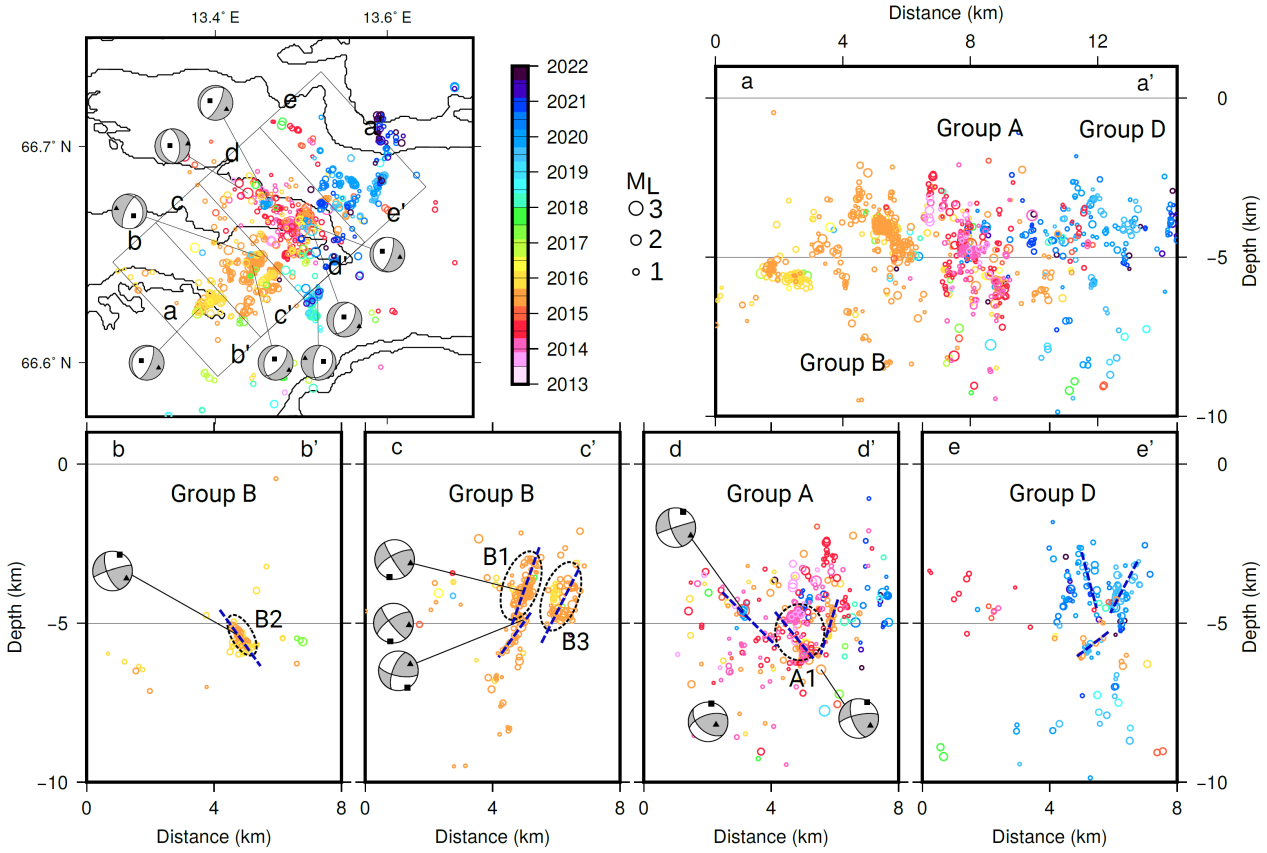

Figure 5. a) Map view of relocated seismicity, focal mechanisms and position of five profiles: strike parallel (a-a') and perpendicular (b-b' - b-b'). b-c) profiles showing the relocated seismicity and focal mechanisms. The relocated earthquakes ($M_L \geq 0$) are shown as open circles colored based on time of occurrence. Focal mechanisms are plotted in cross-section view, with The P- and T-axes shown as black squares and triangles, respectively. Interpreted structures based on seismicity are shown as blue dashed lines. Major clusters are marked with black dashed ellipses. Locations of the profiles are shown in Fig. 5

for their initial absolute locations. To ensure the reliability of our analysis, we only use events below the 95th percentile of the location errors, i.e., less than 1000 meters (for the complete catalog including unrelocated events, see the data availability section).

Our relocation results allow us to resolve the details of the sequence in time and space. Based on location and time we identified four main groups of earthquakes (A, B, C and D) (Fig. 3). Generally, the relocated earthquakes show a similar NE-SW trend. Each group consists of 1-4 individual clusters that each contain ≥ 25 events. We evaluated the event clustering using CC matrices and the links between events using dendrogram. As an example, Fig. 4 shows that group B consists of three individual clusters (B1, B2, and B3), which is consistent with the GrowClust

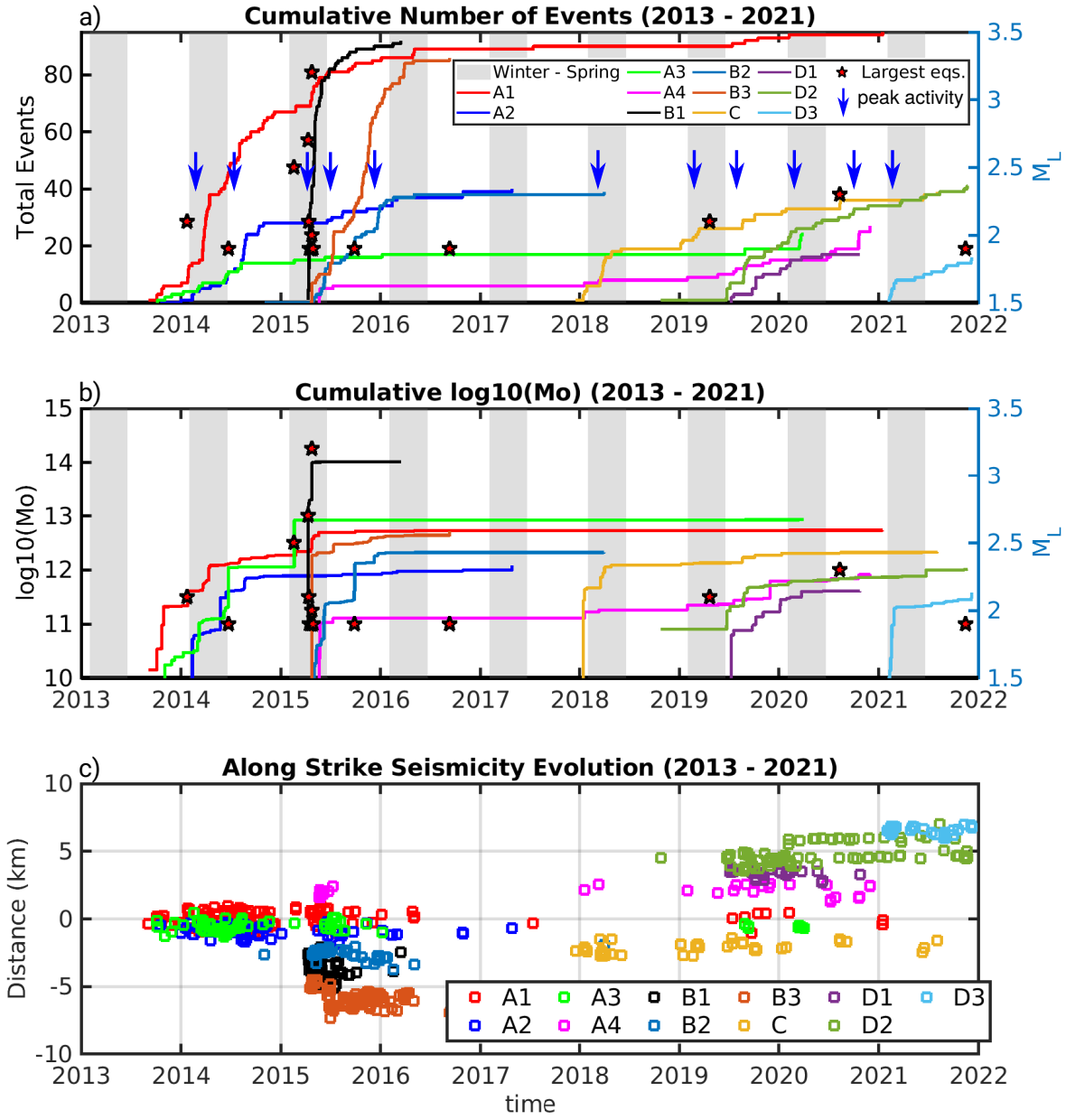

Figure 6. Evolution of the swarm sequences: a) Cumulative number of events for each cluster, shown as solid lines. Blue arrows depict the time when the activity began to increase. Red stars depict the 15 largest events. b) Cumulative log10(Mo) for each cluster. c) Along strike (NNE-SSW) seismicity migration. The earthquake locations relative to the center of cluster A1 are depicted as open circles colored based on their cluster. Only events with $M_L \geq Mc$ are shown here.

clustering result. Swarm activity in Jektvik started in 2013 with Group A, which has remained active throughout the period of investigation. Group A is seen as the center of the swarm and eventually developed into four distinct clusters. Sharp increases in activity for this group were seen in early 2014 and early 2015. Most of the seismicity in this group occurred beneath or nearby

Tjongsfjorden. From 2013 to early 2015, areas outside Group A were relatively quiet, but from April 2015, a new set of earthquakes (Group B) started to appear southwest of Group A. Cluster B1, where the largest event of the whole sequence (M_L 3.2) occurred, was confined in space and time, with most of the seismicity occurring over a two month period. Cluster B2 was located further to the southwest by more than 7 km from the center of Group A and became active a few days after B1. This cluster was also confined in space, but not so much in time, lasting for more than a year. Cluster B3, with an epicentral trend parallel to cluster B1, became active as well during this period, eventually ending in 2016. In 2019, a new patch of seismicity appeared to the southeast of the swarm center forming Group C, which remained active for 3.5 years. Other areas were not very active between 2016 and 2018, although smaller earthquakes would have been missed during this time due to the reduced number of stations. Since 2019, a significant change in the spatial distribution of earthquakes has occurred with the appearance of group D, which is located near the northeastern edge of group A from where it has expanded progressively in a north-northeast direction. By the end of 2021, the Group D hypocenters were located 6.8 km away from the center of Group A. The total extent of the swarm activity is ca. 14 km in SW-NE and ca. 6 km in NW-SE direction, giving a total area of ca. 84 km^2.

We attempted to compute the focal mechanisms of 20 events that occurred after mid-2016, and found two solutions that were deemed acceptable. After mid-2016, stations are fewer, which makes obtaining good solutions challenging. The two solutions from this study, together with those by Michálek et al. (2018) and Shiddiqi et al. (2022) are shown in Fig. 3. They show normal and oblique-normal faulting with strike along NE-SW direction, in agreement with the epicenter trend. The fault planes reveal two possible mechanisms: shallow NW dipping (20 ° - 40 °) and steep SE dipping (50 ° - 70 °) planes. The seismicity profiles in Fig. 5 indicate a number of steeply SE dipping planes in sections b-b' and d-d', which correspond to clusters B2 and A1. The NW shallow dipping mechanisms do not fit with the NW dipping seismicity lineaments, which tend to be steeper. This can be related to the mechanism uncertainty or fault complexity. Therefore, for this plane, we follow the seismicity trends and interpret them as steeply NW dipping planes, which correspond to clusters B1, B2, and A1 (Fig. 5). The stress orientation inferred from the

NE-SW striking parallel normal faults indicate near vertical maximum compression (σ_1) and near horizontal minimum compression (σ_3) in the WNW direction.

To gain better insight into the characteristics of the seismicity, we analyzed the temporal evolution of the cumulative number of events ($M_L \geq Mc$), the cumulative seismic moment (assuming $M_L = M_w$), and the spatio-temporal distribution of along-strike seismicity (Fig. 6). The 15 largest events are also shown in Fig. 6. The occurrence of the largest events, combined with a sequence of sharp increases in cumulative event number and seismic moment, indicate that activity prior to mid-2016 was higher than afterwards. In several clusters, there is a delay between the sharp increases in seismic moment and cumulative event number. The sharp increase in cumulative seismic moment tends to generally occur earlier, which indicates that the larger magnitude events occur relatively early within a swarm and are then followed by many smaller earthquakes. We identified 11 sharp increases in cumulative event number (Fig. 6), with eight of these occurring between February and May, which coincides with the northern hemisphere late winter and spring time (Fig. 6), hinting at a possible seasonality pattern in the seismic activity of the region.

In order to characterise physical properties, we compiled statistics for each cluster (see Table 1): duration, maximum M_L, total seismic moment and the M_w equivalent of all events. We also look at the size of the complete swarm sequence between 2013 and 2021. The total seismic moment for the whole catalog is 1.54 E+14 N.m, which is equivalent to M_w 3.4. We can alternatively estimate the seismic moment from the extent of the faults. The seismicity is distributed onto a number of fault segments, which in total encompass an 11 km NNE-SSW elongated line. If we look in detail at individual segments, for example group B, clusters B1, B2, and B3 cover areas of approximately 9, 5 and 5 km^2, respectively. These correspond to M_w 5.1, 4.9 and 4.9 based on the scaling relationship for SCR earthquakes of Leonard (2010). However, the total moment releases for these clusters correspond to M_w of 3.27, 2.15 and 2.41, which means that only small parts of the fault segments failed.

Table 1. Maximum M_L, total seismic moment and the M_w equivalent of all events for each cluster.

Cluster ID	Duration	Largest ML	Total Mo (N.M)	M_w equivalent
A1	88 months	1.9	5.45E+12	2.4
A2	42 months	1.5	1.21E+12	2.0
A3	77 months	2.5	8.64E+12	2.6
A4	66 months	1.6	8.31E+11	1.9
B1	11 months	3.2	1.03E+14	3.3
B2	12 months	1.9	2.11E+12	2.2
B3	16 months	2.0	5.28E+12	2.4
C	42 months	1.6	2.15E+12	2.2
D1	14 months	1.2	4.05E+11	1.7
D2	36 months	1.5	1.02E+12	1.9
D3	9 months	1.2	3.83E+11	1.7

5 DISCUSSION

The spatio-temporal evolution of the Jektvik swarm sequence shows both distinct patterns in each group and possibly a physical connection between various groups. To better understand the characteristics and causes of the swarm, we address the following questions: 1) How does the sequence fit into the regional geological framework and crustal stress? 2) What triggers the seismicity and causes the seasonality? and 3) How do the clusters interact and influence each other?

The seismicity distribution and focal mechanisms highlight NNE-SSW trending fault zones that are dipping either NW or SE. This trend was previously reported in a geotechnical survey undertaken during the planning phase of a road tunnel (Straumdaltunnelen) (Rostad, H., 1990), where a NNE-SSW trending shear zone and a number of fractures with NNE-SSW and ESE-WNW strikes were identified in the area of our Group B. These orientations are also visible in high resolution Digital Terrain Model images (Figs. S4 and S5, from the Norwegian Mapping Authority (Kartverket))).

Most of the seismic activity is confined to Precambrian granitic and Tonalite gneiss units (Geological Survey of Norway, 2011), which have a high quartz content (e.g., Rutland & Sutherland,

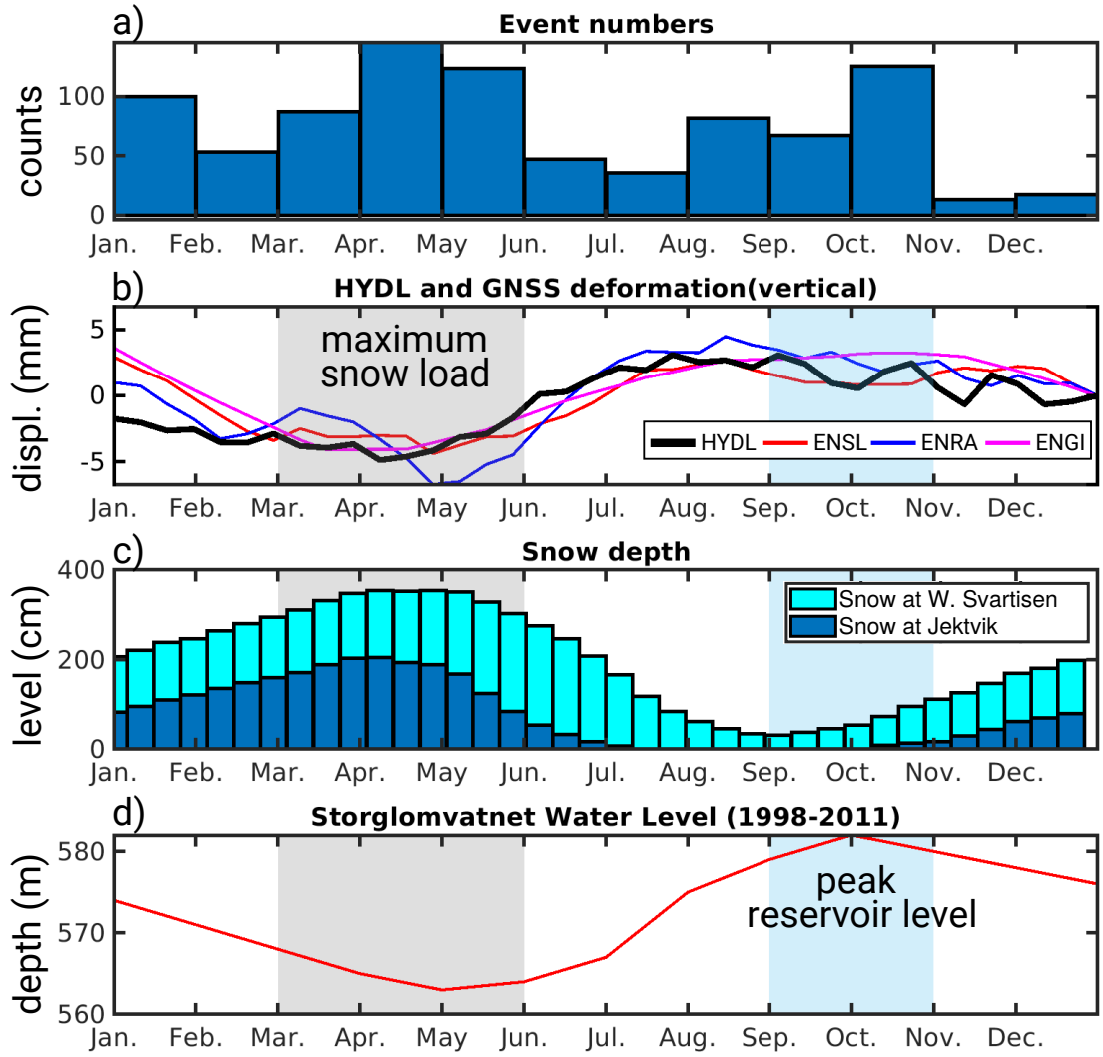

Figure 7. a) Normalized stack of monthly event numbers for the center of Jektvk (Group A). b) Weekly average of vertical displacement from HYDL hydrological loading model (2010-2021) and continuous GNSS (Mid-2019 to Mid-2022) from three stations close to Jektvik region. Linear trend in the GNSS data is removed. c) Weekly average of snow thickness at Jektvik and West Svartisen glacier obtained from SeNorge portal (https://www.senorge.no/). The data are averaged over 10-day intervals. d) Monthly average level of Storglomvatnet water reservoir for the period 1998-2011 obtained from Bønsnes et al. (2015). Time windows with maximum snow load and peak reservoir level are marked as gray and blue areas, respectively. Locations GNSS stations are shown in Fig. 1.a

1967; Castro, 2013). The upper crust of the area has low V_P, which has been linked to a fractured crust and to the presence of fluids (Shiddiqi et al., 2022). Water leakage into a road tunnel is observed several km east of cluster B3 (personal communication, Sølve Utstøl Pettersen, Nordland county), indicating fluid flow within the fracture zones. A shallow refraction seismic profile located

near the tunnel showed that V_P within the fractures dropped 30-40% relative to the surrounding rocks (GEOMAP, 1990). Both a fractured crust and a high quartz content indicate weaknesses in the continental crust where strain can localize and have been previously linked to intraplate seismicity (Lowry & Pérez-Gussinyé, 2011; Costain, 2017). In our case, the earthquakes within the swarms are relatively small compared to the size of the active fault segments, suggesting that they represent failure of relatively small fractures.

The underlying driver of the ongoing deformation and resulting earthquakes is given by the present day stress pattern. As previously shown by Shiddiqi et al. (2022), the stress pattern inferred from fault plane solutions in the area indicates NW-SE extension, where σ_1 is nearly vertical and σ_3 is subhorizontal in NW direction, which favors the reactivation of NNE-SSW structures. As suggested by previous studies (e.g., Bungum et al., 2010; Gradmann et al., 2018), this extension likely arises from a combination of GIA and sediment redistribution, which overcome the regional compressive stress.

From past studies, we have a reasonable understanding of why there are earthquake swarms in Nordland: failure occurs due to local stresses within fracture zones that are likely fluid saturated, with the fluids potentially bringing the faults closer to rupture. But our analysis of seismicity patterns shows that this process is not randomly distributed in space and time. Therefore, we explore the existence of external processes that may trigger and modulate the seismic activity within and between the different clusters. We expect the modulating process to be of natural origin and, therefore, likely to have a seasonal pattern. When looking at the seasonality of the seismicity, we notice a general increase of earthquake numbers in several years between March and May (Fig. 6), corresponding to the end of winter and spring time in Norway. A possible modulating candidate is the change in hydrological load, which has been linked to seismicity in other regions.

The response of the Earth's surface to changes in hydrological load can be observed with geodetic Global Navigation Satellite System (GNSS) data. To investigate the seasonality of the hydrological load, we plotted yearly averaged distributions of normalized earthquake numbers, vertical component GNSS measurements, Hydrological Loading Model (HYDL), snow depth and water reservoir level for the region (Fig. 7). We plotted these datasets in yearly average since

the GNSS data around Jektvik are only available from mid-2019. The selected GNSS stations are located within 50 km of the swarm activity (Fig. 1). After removal of the linear trend, the vertical component of GNSS data is rather constant between July and December, but shows a strong dip, indicating relative subsidence between January and June, which has a maximum amplitude of -10 to -16 mm between March and May. There is a second, but smaller dip between September and November. The GNSS stations have only been operational for less than three years, but we consider the signals reliable as a similar seasonal pattern (although with different amplitudes) is seen on GNSS stations in the broader region of northern Scandinavia (as shown in http://geodesy.unr.edu/NGLStationPages/gpsnetmap/GPSNetMap.html). HYDL is a crustal deformation model derived from global hydrological constraints (Dill & Dobslaw, 2013). For the Jektvik region, it shows the same seasonal pattern as the GNSS data with an estimated maximum ground vertical displacement of -8 mm. The small mismatch between the GNSS data and HYDL estimates is due to the low resolution of the hydrological load model. While the vertical displacement is affected by different processes (e.g., tides (Drouin et al., 2016), rainfall (Hsu et al., 2021)), our assumption is that the main signal of relative subsidence during March-May is caused by the regional snow load, while the secondary signal during September-November could be caused by the maximum filling of water reservoirs in the autumn (as seen for the Storglomvatnet reservoir shown in Fig. 7).

The seasonal peak in seismicity that we identify in Fig. 7.a coincides with the maximum hydrological load that we ascribe to snow accumulation in the winter. Hydrological loads can be significant enough to cause elastic ground deformation, alter tectonic stress and modulate seismicity, as shown for northeastern Japan by Heki (2003). To test the significance of the static load change from snow accumulation in the area, we follow (Deng et al., 2010; Büyükakpınar et al., 2021) and model 3-D Coulomb failure stress changes (ΔCFF). We computed the 3-D stress tensor due to surface loading on a half-space elastic media using Boussinesq-Cerruti solutions (see Deng et al., 2010). We used a simple snow thickness model that contains two peaks: 2 meters in Jektvik and 4 meters in the Svartisen glacier area (Fig. 8). Then we computed the changes in shear

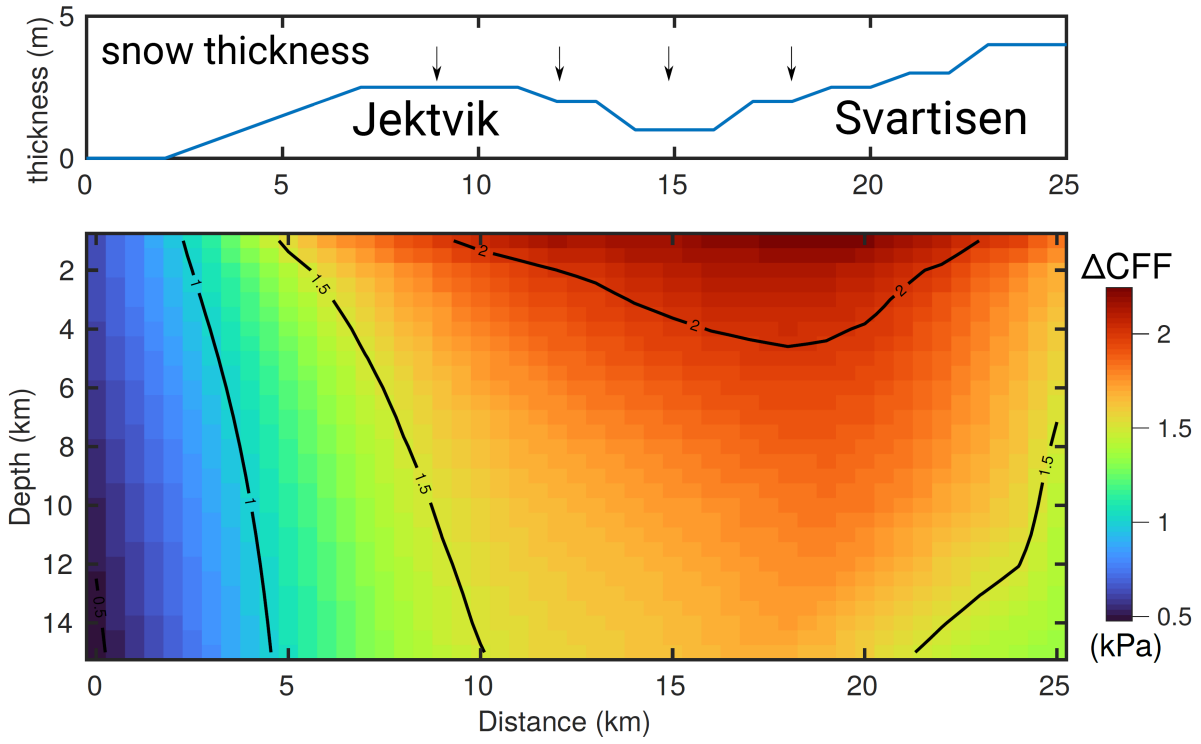

Figure 8. ΔCFF modeling result using a simple snow thickness model consists of two peaks in Jektvik and Svartisen. a) 2-D profile of the snow thickness used to calculate the ΔCFF due to snow load. b) ΔCFF resolved on normal faults beneath Jektvik and Svartisen. Black lines are contours of ΔCFF with 0.5 kPa interval.

($\Delta\tau$) and normal stresses ($\Delta\sigma_n$) for a 45° dip and -90° rake receiver fault due the load. Ignoring the pore-pressure change, ΔCFF is defined as

$$\Delta CFF = \Delta\tau + \mu\Delta\sigma_n \tag{2}$$

where μ is the friction coefficient that is assumed to be 0.6. From this modeling, we found that snow load increases the ΔCFF on normal faults (Fig. 8) in Jektvik by 1.5 to 1.8 kPa at depth of up to 8 km. We consider that these changes in hydrological loading are sufficient to trigger seismicity through stress and pore pressure changes (Deng et al., 2010; Büyükakpınar et al., 2021), even though they are quite small. Previous studies show that small ΔCFF variations (a few kPa) are able to modulate the seismicity (Christiansen et al., 2007; Pollitz et al., 2013; Craig et al., 2017).

The stress modulation affects a larger region, but it can only trigger fault system that are critically stressed and optimally oriented. In the case of Jektvik, such hydrological load is efficient

in triggering seismicity owing to the existence of an intricate network of steeply dipping normal faults at shallow depth. With a near vertical σ_1 direction, an increase in hydrological load enhances the tectonic stress most efficiently. While the hydrological load changes present a tenable trigger mechanism for seismicity in our case, additional work will be needed to model pore-pressure changes and to understand the relative contribution from different processes such as snow cover over the broader region versus higher snow accumulation on glaciers, the filling of reservoirs and changes in the ocean loading.

While the hydrological load change appears to be a likely seismicity modulating trigger mechanism, the spatio-temporal evolution of the Jektvik seismicity indicates further interaction and triggering within and between clusters, which can be explained by co-seismic ΔCFF. Clusters of small to moderate earthquakes can increase Coulomb stress on faults within or on neighboring segments and bring them closer to failure (Gahalaut et al., 2004; Hauksson et al., 2017). In addition to ΔCFF, co-seismic pore-pressure increase caused by earthquakes in one segment can reduce the normal stress, hence can increase the ΔCFF.

In order to understand the ΔCFF effect due to earthquakes in one cluster on to the seismogenic faults of other clusters, we performed simple but representative modeling using the Coulomb 3.3 software (Lin & Stein, 2004; Toda et al., 2005), ignoring the possibility of co-seismic pore-pressure change. We used a cumulative fault source in a cluster following the approach of Gahalaut et al. (2004, 2022). We modeled ΔCFF due to slip on the NNE-SSW oriented normal fault, simulating a typical earthquake cluster source of the Jektvik swarm. We used the maximum cumulative M_0 of 1.03E+14, which is equivalent to M_w 3.3. Based on the scaling relation for SCR dip-slip earthquakes of Leonard (2010), we used a length of 400 m and downdip width of the source fault as 400 m, and assumed a normal slip of 2 cm. We resolved ΔCFF on faults with orientation similar to the source fault. As expected, the modeling result shows increasing ΔCFF at the tip of the source faults (King et al., 1994). This implies that ΔCFF will increase on normal fault segments which are sub-parallel and are almost aligned with the source fault (Fig. 9). This simple model can explain the fault interaction through stress transfer and triggering of seismic events in between clusters. For example, cumulative ΔCFF generated by events in cluster A1 can trigger seismicity

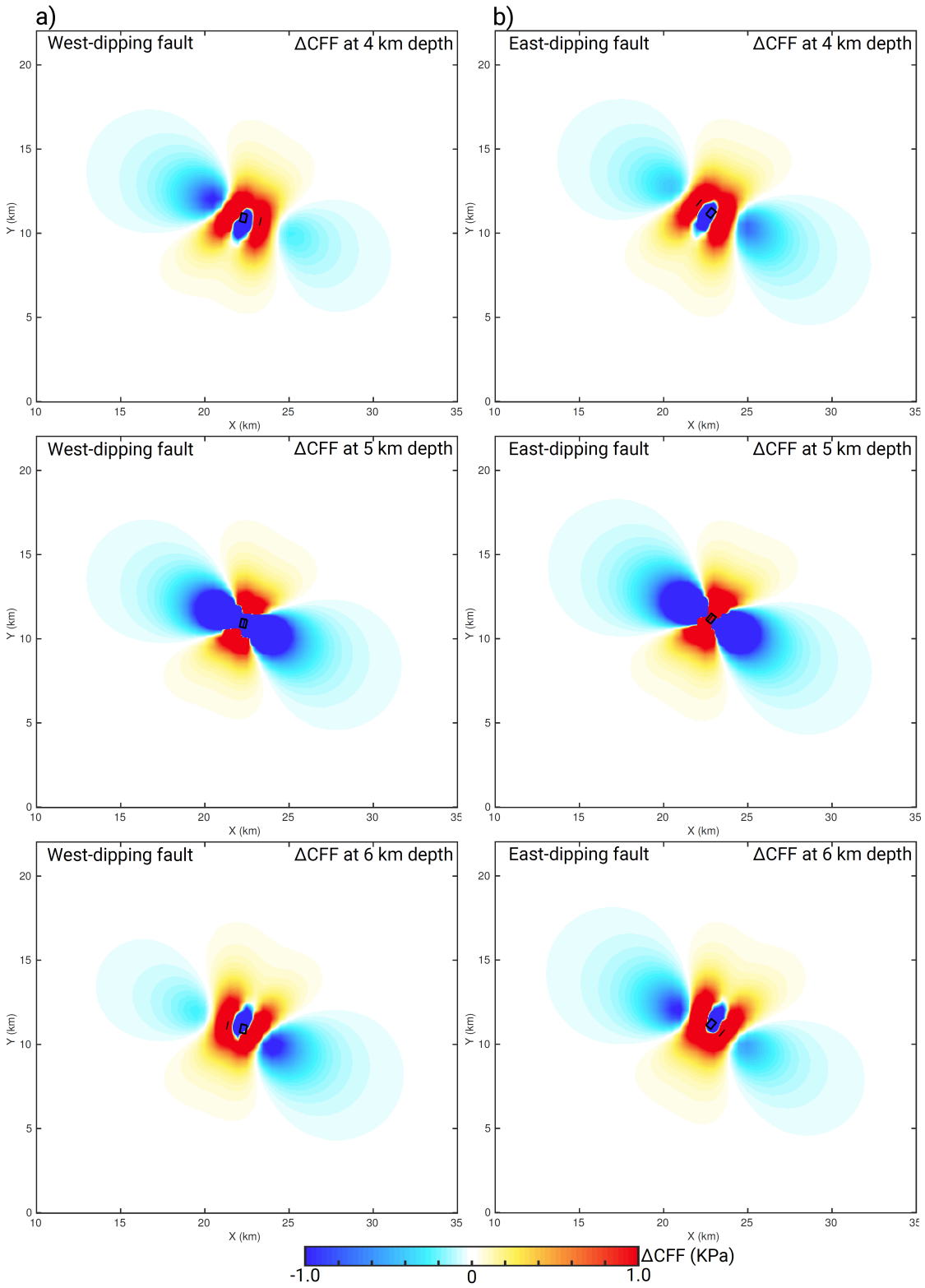

Figure 9. Coulomb stress change (ΔCFF) using a typical normal faulting earthquake in Jetkvik to show the possible inter-cluster triggering. The modeling was performed using using a normal event with M_w 3.3 with NNE-SSW strike. The ΔCFF are computed for west- and east-dipping planes with normal motion at 4, 5 and 6 km depth.

in clusters A4, B1, B3 and possibly later events in group D. Additionally, triggering of parallel segments will be effective if the receiver faults are shallower or deeper than the source faults. This condition can explain the triggering of clusters A2 and A3 due to cumulative ΔCFF from cluster A1.

In light of the ΔCFF modeling, we hypothesize that seasonal load changes are able to trigger and modulate the seismicity. Once a cluster becomes active, it can possibly trigger earthquakes in neighboring clusters. These processes help to promote seismic rupture where the fracture system is already in a critically stressed state in response to present day stresses. Therefore, small increase in ΔCFF can trigger the swarm activity. Pore-pressure changes due to load changes and co-seismic processes are likely to play a role and can further promote failure (Gahalaut et al., 2022). However, given that hydrological loading appears to be the dominant times-dependent process and considering location uncertainties, it is not possible to test the contribution of additional processes on this complex swarm sequence using widely used modelling schemes (e.g., Shapiro et al., 1997; Shapiro, 2015).

6 CONCLUSIONS

We present detailed spatio-temporal and seismogenesis characterisation of a seismic swarm sequence in Jektvik, northern Norway, using an enhanced earthquake catalog that spans a period of nine years. As expected for earthquake swarm activity, the affected area is large but the overall moment release is relatively small. In this case, the active area was ca. 84 km^2, but the maximum earthquake magnitude was only M_L 3.2. The hypocenters were relocated and clustered using differential time data and waveform cross-correlation. The swarms occurred within an intricate system of NNE-SSW striking fluid-saturated fracture zones, where the earthquakes themselves are seen as failure of smaller fractures that are aligned with the orientation of the zones. This is apparent from the NNE-SSW trending normal fault mechanisms, which are a result of local extensional stresses, and from the alignment of seismicity in the region. The seismicity trend matches the surface lineaments that are seen on high resolution terrain models. Based on precise locations and origin times, we combined earthquake clusters into four main groups. The relocated seismicity

shows distinct spatio-temporal patterns within and in between the groups. The seismic activity expanded progressively from the center, first toward SW and later toward east and NE. While the center of the sequence remained active during the entire observation period, the neighboring segments were mostly active only for a limited time.

Based on the coincidence of times of highest seismic activity and maximum hydrological load, we hypothesize that the hydrological load acts as a seasonal modulator. The seismic activity tends to increase between February and May, at the end of the northern hemisphere winter and beginning of spring. Vertical components of GNSS data show a maximum subsidence during this period, which correlates with the peak of snow load in the region. We show that the snow load increases the ΔCFF on the normal fault system and is possibly responsible for the seasonal modulation of seismicity. The response of each segment to this load is different, reflecting the ambient stress heterogeneity and fault characteristics. We further invoke the co-seismic ΔCFF as an additional process that promotes failure within and between fault segments.

ACKNOWLEDGMENTS

The study was supported by funding from the Research Council of Norway for the project “IPSIN - Intraplate Seismicity in India and Norway: Distribution, properties and causes”. The authors VKG, RKY and KG acknowledge the support from the IPSIN Project (MOES/India-Nor/PS-3(GH)/2015). The author S.C. acknowledges support from the Portuguese FCT – Fundação para a Ciência e a Tecnologia, I.P., within the scope of project PTDC/CTA-GEF/6674/2020. We thank Odleiv Olesen and Sofie Gradmann from the Geological Survey of Norway for discussion on geology of Nordland. We thank Sølve Utstøl Pettersen, Nordland Fylkeskommune, for providing geotechnical information and technical reports on Straumdaltunnelen (Straumdal tunnel) near the study area. We acknowledge the operators of permanent and temporary seismic networks used in this study: NNSN (NS; https://doi.org/10.7914/SN/NS) , Neonor2 (2G), and Scanlips3D (ZR; https://doi.org/10.7914/SN/ZR_2013).

DATA AVAILABILITY

Earthquake data catalog from the Norwegian National Seismic Network (NNSN) is available at NNSN webpage (https://nnsn.geo.uib.no/nnsn/#/data/events/bulletins). Seismic data from NNSN (network code: NS) (Ottemöller et al., 2021) and Neonor2 (2G) (Michálek et al., 2018) are available at UiB-Norsar European Integrated Data Archive (EIDA) Node webpage (https://nnsn.geo.uib.no/nnsn/#/data/waveforms/access). Seismic data for Scanlips3D (ZR) (England et al., 2016) network are archived at the Incorporated Research Institutions for Seismology (IRIS) Data Management Center (DMC) (http://ds.iris.edu/ds/nodes/dmc/). Earthquake data were processed using EQtransformer package (https://eqtransformer.readthedocs.io), eqcorrscan package (https://eqcorrscan.readthedocs.io), Obspy package (https://docs.obspy.org/) and Seisan earthquake analysis software (http://seisan.info/). The Norwegian bedrock geology map (Geological Survey of Norway, 2011) is available at Geological Survey of Norway portal (https://geo.ngu.no/kart/berggrunn_mobil). Digital Terrain Model images are available at Norwegian mapping authority (Kartverket) portal (https://hoydedata.no/LaserInnsyn/ and https://www.geonorge.no/). The HYDL model is available at ftp://esmdata.gfz-potsdam.de/LOADING. Snow depth data is available at SeNorge portal (https://www.senorge.no/). The processed GNSS data are available from Nevada Geodetic Laboratory webpage (http://geodesy.unr.edu/magnet.php). Figures in this article were created using Matlab (https://www.mathworks.com/products/matlab.html), Generic Mapping Tools (Wessel et al., 2013), QGIS software (QGIS Development Team, 2021) and Inkscape, a vector graphics editor (https://inkscape.org/). Earthquake catalog generated in this study is available at at Zenodo https://doi.org/10.5281/zenodo.7101184.

References

Alsaker, A., Kvamme, L. B., Hansen, R. A., Dahle, A., & Bungum, H., 1991. The ML scale in Norway, *Bulletin of the Seismological Society of America*, **81**(2), 379–398.

Atakan, K., Lindholm, C. D., & Havskov, J., 1994. Earthquake swarm in Steigen, northern Norway: an unusual example of intraplate seismicity, *Terra Nova*, **6**(2), 180–194.

Beyreuther, M., Barsch, R., Krischer, L., Megies, T., Behr, Y., & Wassermann, J., 2010. ObsPy: A Python Toolbox for Seismology, *Seismological Research Letters*, **81**(3), 530–533.

Bisrat, S., DeShon, H. R., & Rowe, C., 2012. Microseismic Swarm Activity in the New Madrid Seismic Zone, *Bulletin of the Seismological Society of America*, **102**(3), 1167–1178.

Bønsnes, T. E., Elvehøy, H., Vatne, A., & Kvambekk, Å., 2015. Oppdragsrapport A: Storglomfjordutbyggingen Hydrologiske undersøkelser i 2014.

Bungum, H. & Olesen, O., 2005. The 31st of August 1819 Lurøy earthquake revisited, *Norwegian Journal of Geology*, (85), 245–252.

Bungum, H., Hokland, B. K., Husebye, E. S., & Ringdal, F., 1979. An exceptional intraplate earthquake sequence in Meløy, Northern Norway, *Nature*, (280), 32–35.

Bungum, H., Vaage, S., & Husebye, E. S., 1982. The Meløy earthquake sequence, northern Norway: source parameters and their scaling relations, *Bulletin of the Seismological Society of America*, **72**(1), 197–206.

Bungum, H., Olesen, O., Pascal, C., Gibbons, S., Lindholm, C., & Vestøl, O., 2010. To what extent is the present seismicity of Norway driven by post-glacial rebound?, *Journal of the Geological Society*, **167**(2), 373–384.

Büyükakpınar, P., Cesca, S., Hainzl, S., Jamalreyhani, M., Heimann, S., & Dahm, T., 2021. Reservoir-Triggered Earthquakes Around the Atatürk Dam (Southeastern Turkey), *Frontiers in Earth Science*, **9**.

Castro, A., 2013. Tonalite–granodiorite suites as cotectic systems: A review of experimental studies with applications to granitoid petrogenesis, *Earth-Science Reviews*, **124**, 68–95.

Chamberlain, C. J., Hopp, C. J., Boese, C. M., Warren-Smith, E., Chambers, D., Chu, S. X., Michailos, K., & Townend, J., 2017. EQcorrscan: Repeating and Near-Repeating Earthquake Detection and Analysis in Python, *Seismological Research Letters*, **89**(1), 173–181.

Christiansen, L. B., Hurwitz, S., & Ingebritsen, S. E., 2007. Annual modulation of seismicity along the san andreas fault near parkfield, ca, *Geophysical Research Letters*, **34**(4).

Corfu, F., Andersen, T. B., & Gasser, D., 2014. The Scandinavian Caledonides: main features, conceptual advances and critical questions, *Geological Society, London, Special Publications*,

390(1), 9–43.

Costain, J. K., 2017. Groundwater recharge as the trigger of naturally occurring intraplate earthquakes, *Geological Society, London, Special Publications*, **432**(1), 91–118.

Craig, T. J., Chanard, K., & Calais, E., 2017. Hydrologically-driven crustal stresses and seismicity in the New Madrid Seismic Zone, *Nature Communications*, **8**(1), 2143.

Demuth, A., Ottemöller, L., & Keers, H., 2019. QLg wave tomography beneath Norway, *Journal of Seismology*, **23**, 151–164.

Deng, K., Zhou, S., Wang, R., Robinson, R., Zhao, C., & Cheng, W., 2010. Evidence that the 2008 Mw 7.9 Wenchuan earthquake could not have been induced by the Zipingpu reservoir, *Bulletin of the Seismological Society of America*, **100**(5B), 2805–2814.

Dill, R. & Dobslaw, H., 2013. Numerical simulations of global-scale high-resolution hydrological crustal deformations, *Journal of Geophysical Research: Solid Earth*, **118**(9), 5008–5017.

Drouin, V., Heki, K., Sigmundsson, F., Hreinsdóttir, S., & Ófeigsson, B. G., 2016. Constraints on seasonal load variations and regional rigidity from continuous GPS measurements in Iceland, 1997–2014, *Geophysical Journal International*, **205**(3), 1843–1858.

England, R. W., Ebbing, J., & Ben-Mansour, W., 2016. SCANdinavian LIthosphere P and S wave experiment 3 D, Tech. rep.

Fossen, H., 2010. Extensional tectonics in the North Atlantic caledonides: a regional view, in *Continental tectonics and mountain building: the legacy of Peach and Horne*, Geological Society of London.

Gahalaut, K., Gahalaut, V., Bandari, N., Shekar, M., Tc, S., & Srinagesh, D., 2022. Long duration non-volcanic and non-tectonic palghar earthquake swarm in the stable continental region of india—role of seasonal rainfall and earthquake cascading, *Journal of Seismology*.

Gahalaut, V. K., Kalpna, & Singh, S. K., 2004. Fault interaction and earthquake triggering in the koyna-warna region, india, *Geophysical Research Letters*, **31**(11).

Geological Survey of Norway, 2011. Nasjonal berggrunnsdatabase.

GEOMAP, 1990. RV. 17 Tunnel Reppen - Strømdal: Resfraksjonsseismiske Målinger 1990 (In Norwegian), Tech. rep.

Gibbons, S. J., Bøttger Sørensen, M., Harris, D. B., & Ringdal, F., 2007. The detection and location of low magnitude earthquakes in northern Norway using multi-channel waveform correlation at regional distances, *Physics of the Earth and Planetary Interiors*, **160**(3), 285–309.

Gradmann, S., Olesen, O., Keiding, M., & Maystrenko, Y., 2018. *The Regional 3d Stress Field of Nordland, Northern Norway - Insights from Numerical Modelling*, chap. Neotectonics in Nordland - Implications for petroleum exploration (NEONOR2), Geological Survey of Norway, Trondheim.

Hainzl, S., Kraft, T., Wassermann, J., Igel, H., & Schmedes, E., 2006. Evidence for rainfall-triggered earthquake activity, *Geophysical Research Letters*, **33**(19).

Hauksson, E., Meier, M.-A., Ross, Z. E., & Jones, L. M., 2017. Evolution of seismicity near the southernmost terminus of the San Andreas Fault: Implications of recent earthquake clusters for earthquake risk in southern California, *Geophysical Research Letters*, **44**(3), 1293–1301.

Havskov, J. & Ottemoller, L., 1999. SeisAn Earthquake Analysis Software, *Seismological Research Letters*, **70**(5), 532–534.

Havskov, J. & Ottemöller, L., 2010. *Routine Data Processing in Earthquake Seismology: With Sample Data, Exercises and Software*, Springer.

Havskov, J., Voss, P. H., & Ottemöller, L., 2020. Seismological Observatory Software: 30 Yr of SEISAN, *Seismological Research Letters*, **91**(3), 1846–1852.

Heki, K., 2003. Snow load and seasonal variation of earthquake occurrence in japan, *Earth and Planetary Science Letters*, **207**(1), 159–164.

Hicks, E. C., Bungum, H., & Lindholm, C. D., 2000. Seismic activity, inferred crustal stresses and seismotectonics in the Rana region, Northern Norway, *Quaternary Science Reviews*, **19**(14), 1423 – 1436.

Hsu, Y.-J., Kao, H., Bürgmann, R., Lee, Y.-T., Huang, H.-H., Hsu, Y.-F., Wu, Y.-M., & Zhuang, J., 2021. Synchronized and asynchronous modulation of seismicity by hydrological loading: A case study in Taiwan, *Science Advances*, **7**(16), eabf7282.

Janutyte, I., Lindholm, C., & Olesen, O., 2017. Earthquake source mechanisms in onshore and offshore Nordland, northern Norway, *Norwegian Journal of Geology*, **97**(3), 227–239.

Jiang, C., Zhang, P., White, M. C. A., Pickle, R., & Miller, M. S., 2022. A Detailed Earthquake Catalog for Banda Arc–Australian Plate Collision Zone Using Machine-Learning Phase Picker and an Automated Workflow, *The Seismic Record*, **2**(1), 1–10.

Kierulf, H. P., 2017. Analysis strategies for combining continuous and episodic GNSS for studies of neo-tectonics in Northern-Norway, *Journal of Geodynamics*, **109**, 32 – 40.

Kierulf, H. P., Steffen, H., Simpson, M. J. R., Lidberg, M., Wu, P., & Wang, H., 2014. A GPS velocity field for Fennoscandia and a consistent comparison to glacial isostatic adjustment models, *Journal of Geophysical Research: Solid Earth*, **119**(8), 6613–6629.

King, G. C. P., Stein, R. S., & Lin, J., 1994. Static stress changes and the triggering of earthquakes, *Bulletin of the Seismological Society of America*, **84**(3), 935–953.

Krischer, L., Megies, T., Barsch, R., Beyreuther, M., Lecocq, T., Caudron, C., & Wassermann, J., 2015. ObsPy: A bridge for seismology into the scientific Python ecosystem, *Computational Science Discovery*, **8**, 014003.

Leonard, M., 2010. Earthquake Fault Scaling: Self-Consistent Relating of Rupture Length, Width, Average Displacement, and Moment Release, *Bulletin of the Seismological Society of America*, **100**(5A), 1971–1988.

Lienert, B. R. & Havskov, J., 1995. A computer program for locating earthquakes both locally and globally, *Seismological Research Letters*, **66**(5), 26–36.

Lin, J. & Stein, R. S., 2004. Stress triggering in thrust and subduction earthquakes and stress interaction between the southern san andreas and nearby thrust and strike-slip faults, *Journal of Geophysical Research: Solid Earth*, **109**(B2).

Lowry, A. R. & Pérez-Gussinyé, M., 2011. The role of crustal quartz in controlling Cordilleran deformation, *Nature*, **471**(7338), 353–357.

Luckett, R., Ottemöller, L., Butcher, A., & Baptie, B., 2018. Extending local magnitude ML to short distances, *Geophysical Journal International*, **216**(2), 1145–1156.

Mäntyniemi, P. B., Sørensen, M. B., Tatevossian, T. N., Tatevossian, R. E., & Lund, B., 2020. A reappraisal of the Lurøy, Norway, earthquake of 31 August 1819, *Seismological Research Letters*.

Megies, T., Krischer, L., Chambers, D. J., Eulenfeld, T., Chamberlain, C. J., Lecocq, T., & Barsch, R., 2019. ObsPy - A Python Library for Seismology, in *AGU Fall Meeting Abstracts*, vol. 2019, pp. NS21A–12.

Michálek, J., Tjåland, N., Drottning, A., Strømme, M. L., Storheim, B. M., Rondenay, S., & Ottemöller, L., 2018. *Report on seismic observations within the NEONOR2 project in the Nordland region, Norway (Aug. 2013 - May 2016)*, chap. Neotectonics in Nordland - Implications for petroleum exploration (NEONOR2), Geological Survey of Norway, Trondheim.

Mousavi, S. M., Sheng, Y., Zhu, W., & Beroza, G. C., 2019. STanford EArthquake Dataset (STEAD): A Global Data Set of Seismic Signals for AI, *IEEE Access*, **7**, 179464–179476.

Mousavi, S. M., Ellsworth, W., Weiqiang, Z., Chuang, L., & Beroza, G., 2020. Earthquake transformer—an attentive deep-learning model for simultaneous earthquake detection and phase picking, *Nature Communications*, **11**, 3952.

Muir-Wood, R., 1989. The Scandinavian earthquakes of 22 December 1759 and 31 August 1819, *Disasters*, (412), 223–236.

Münchmeyer, J., Woollam, J., Rietbrock, A., Tilmann, F., Lange, D., Bornstein, T., Diehl, T., Giunchi, C., Haslinger, F., Jozinović, D., Michelini, A., Saul, J., & Soto, H., 2022. Which picker fits my data? a quantitative evaluation of deep learning based seismic pickers, *Journal of Geophysical Research: Solid Earth*, **127**(1), e2021JB023499.

Ottemöller, L., Strømme, M. L., & Storheim, B. M., 2018. *Seismic monitoring and data processing at the Norwegian National Seismic Network*, vol. 52, chap. Summary of the Bulletin of the International Seismological Centre 2015 January-June, pp. 27–40, International Seismological Centre, Thatcham, United Kingdom.

Ottemöller, L., Michálek, J., Christensen, J., Baadshaug, U., Halpaap, F., Natvik, o., Kværna, T., & Oye, V., 2021. UiB-NORSAR EIDA Node: Integration of Seismological Data in Norway, *Seismological Research Letters*, **92**(3), 1491–1500.

Pollitz, F. F., Wech, A., Kao, H., & Bürgmann, R., 2013. Annual modulation of non-volcanic tremor in northern cascadia, *Journal of Geophysical Research: Solid Earth*, **118**(5), 2445–2459.

QGIS Development Team, 2021. *QGIS Geographic Information System*, QGIS Association.

Roberts, D., 1988. The terrane concept and the Scandinavian Caledonides: a synthesis, *Norges Geologiske Undersøkelse Bulletin*, (413), 93–99.

Ross, Z. E., Cochran, E. S., Trugman, D. T., & Smith, J. D., 2020. 3D fault architecture controls the dynamism of earthquake swarms, *Science*, **368**(6497), 1357–1361.

Rostad, H., 1990. Strømdal Tunnel Sør: Ingeior Geologisk Rapport (In Norwegian), Tech. rep.

Rutland, R. W. R. & Sutherland, D. S., 1967. The chemical Composition of Granitic Gneisses and Spragmitic Meta-Sediments in the Glomfjord Region, Northern Norway., *Norsk Geologisk Tidsskrift*, **47**(4), 359–374.

Shapiro, S. A., 2015. *Fluid-Induced Seismicity*, Cambridge University Press.

Shapiro, S. A., Huenges, E., & Borm, G., 1997. Estimating the crust permeability from fluid-injection-induced seismic emission at the KTB site, *Geophysical Journal International*, **131**(2), F15–F18.

Sharma, V., Wadhawan, M., Rana, N., Sreejith, K., Agrawal, R., Kamra, C., Hosalikar, K., Narkhede, K. V., Suresh, G., & Gahalaut, V. K., 2020. A long duration non-volcanic earthquake sequence in the stable continental region of India: The Palghar swarm, *Tectonophysics*, **779**, 228376.

Shiddiqi, H. A., Tun, P. P., & Ottemöller, L., 2019. Minimum 1D Velocity Model and Local Magnitude Scale for Myanmar, *Seismological Research Letters*, **90**(5), 1923–1936.

Shiddiqi, H. A., Ottemöller, L., Rondenay, S., Halpaap, F., Gradmann, S., & Michálek, J., 2022. Crustal structure and intraplate seismicity in Nordland, Northern Norway: Insight from Seismic Tomography, *Geophysical Journal International*, **230**, 813–830.

Snoke, J. A., 2003. FOCMEC: Focal mechanism determinations, *International Handbook of Earthquake and Engineering Seismology*, **85**, 1629–1630.

Snoke, J. A., 2017. *FOCMEC: FOCal MEChanism Determinations Manual*.

Springer, A., Karegar, M. A., Kusche, J., Keune, J., Kurtz, W., & Kollet, S., 2019. Evidence of daily hydrological loading in gps time series over europe, *Journal of Geodesy*, **93**(10), 2145–2153.

Talwani, P., 2017. On the nature of intraplate earthquakes, *Journal of Seismology*, **21**(1), 47–68.

Toda, S., Stein, R. S., Richards-Dinger, K., & Bozkurt, S. B., 2005. Forecasting the evolution of seismicity in southern california: Animations built on earthquake stress transfer, *Journal of Geophysical Research: Solid Earth*, **110**(B5).

Trugman, D. T. & Shearer, P. M., 2017. Growclust: A hierarchical clustering algorithm for relative earthquake relocation, with application to the spanish springs and sheldon, nevada, earthquake sequences, *Seismological Research Letters*, **88**(2A), 379–391.

Wessel, P., Smith, W. H. F., Scharroo, R., Luis, J., & Wobbe, F., 2013. Generic mapping tools: Improved version released, *Eos, Transactions American Geophysical Union*, **94**(45), 409–410.

submitted to *Geophys. J. Int.*

Supporting information for "Seismicity modulation due to hydrological loading in a stable continental region: a case study from the Jektvik swarm sequence in Northern Norway"

Hasbi Ash Shiddiqi[1], Lars Ottemöller[1], Stéphane Rondenay[1], Susana Custódio[2], Vineet K. Gahalaut[3], Rajeev K. Yadav[3], Felix Halpaap[1], and Kalpna Gahalaut[3]

[1] *Department of Earth Science, University of Bergen, Bergen, Norway.*

[2] *Instituto Dom Luiz, Faculdade de Ciências, Universidade de Lisboa, Lisboa, Portugal.*

[3] *CSIR-National Geophysical Research Institute, Hyderabad, India.*

October 10, 2022

Contents

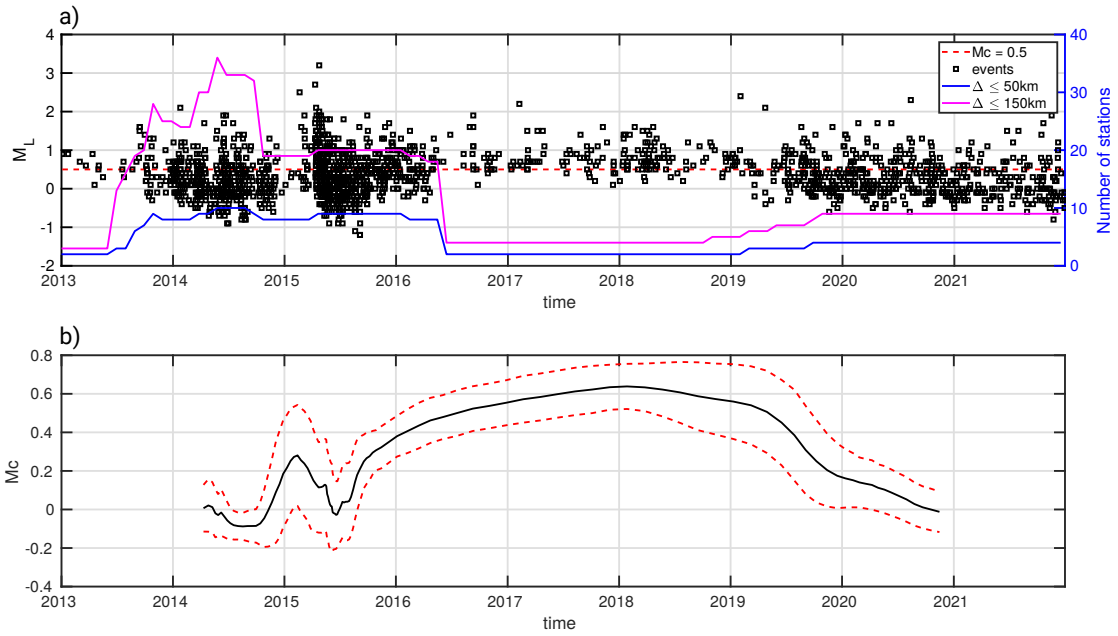

Figure S1. a) Time series plot of M_L and number of stations within 50 and 150 km radius from the center of Jektvik area. The period with the highest number of stations are between mid 2013 and mid 2016 during a number of temporary deployments. The number of stations dropped significantly between mid 2016 and late 2018, resulting in fewer small magnitude events. The number of station is increasing again since late 2018, which is shown by the reduction of detection threshold. b) Time evolution of Magnitude completeness (Mc) reflecting the changes in the station numbers. The Mc become the highest between mid 2016 to late 2019, when the station number is less. The Mc is computed using a sampling window of 400 earthquakes in the ZMAP matlab package (ref.). The solid black and dashed red lines represent the Mc and its error ranges, respectively.

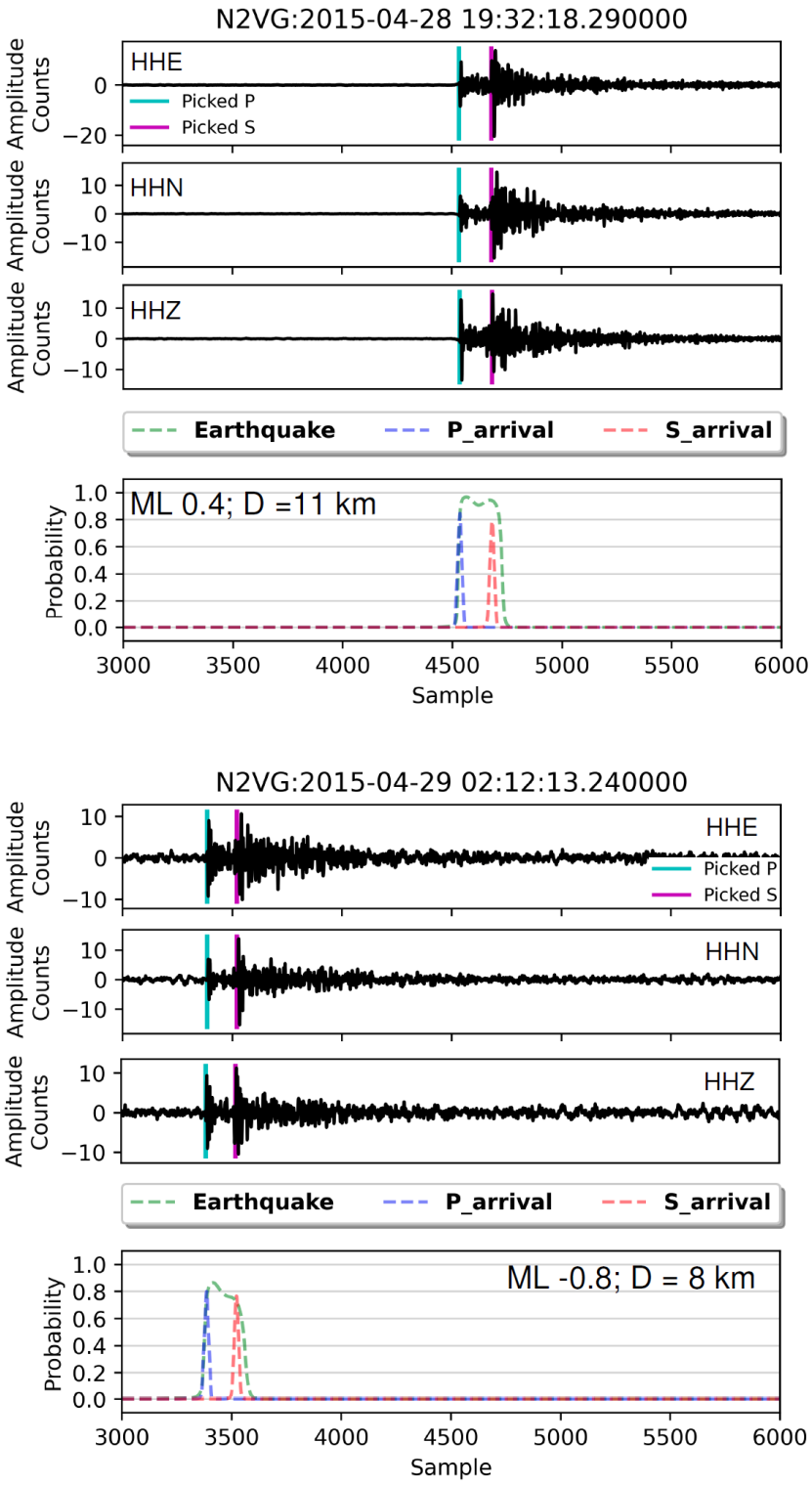

Figure S2. Eqtransformer event detection and picking examples for M_L 0.4 and M_L -0.8 events recorded on N2VG station. For each event, the first three panels are the traces in E-W, N-S and vertical components, and the fourth panel shows the probability associated with earthquake signal, P- and S-arrivals.

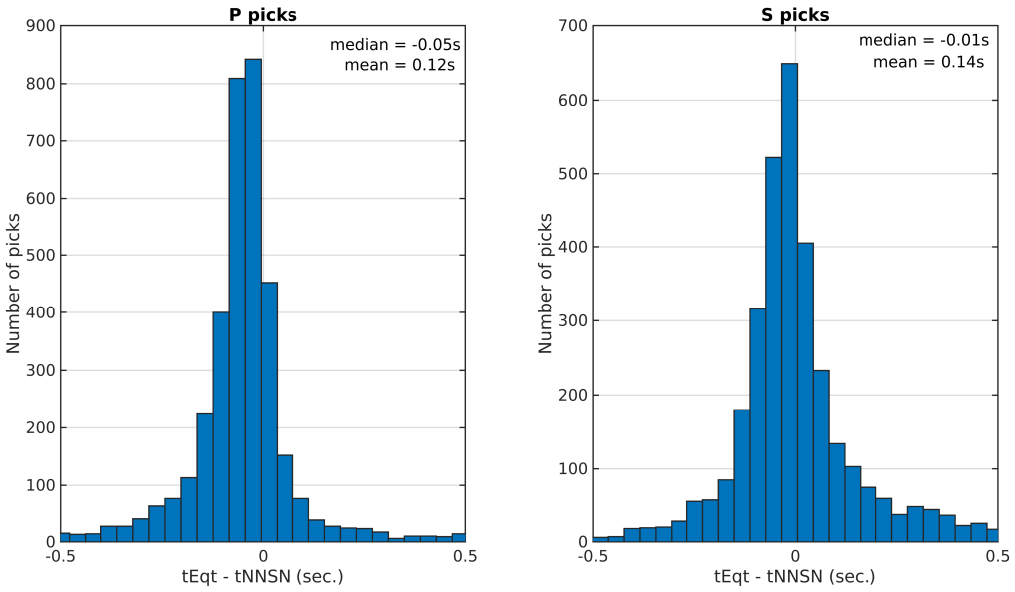

Figure S3. Difference between P- and S-picks from Eqtransformer and from the NNSN catalog. The mean of absolute difference for P-picks are 0.12 s and for S-picks are 0.14 s.

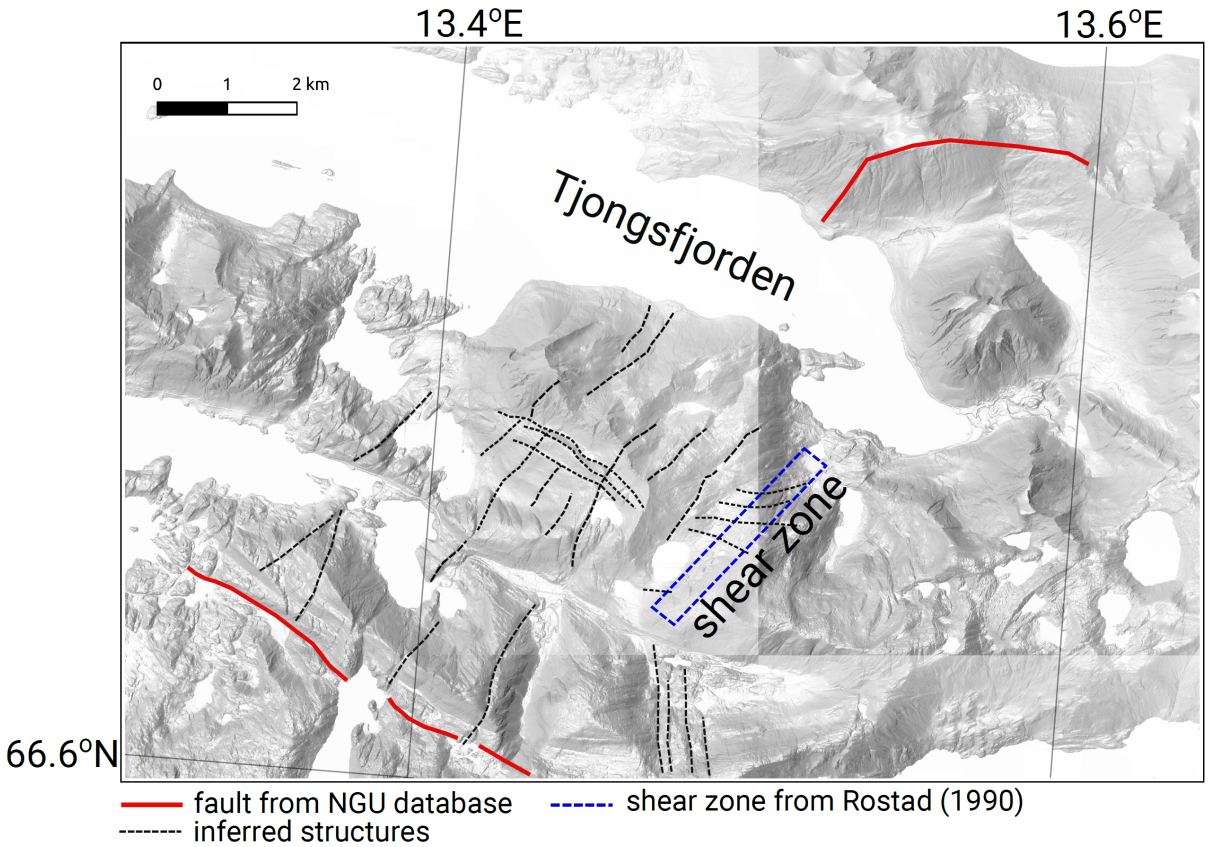

Figure S4. Digital terrain model (DTM) for Jektvik area derived. Interpreted structures are shown as dashed black. Approximate location of a shear zone reported by (Rostad, H., 1990) is shown as blue dashed box. Faults reported in the National bedrock database provided by the Geological Survey of Norway (NGU) (Geological Survey of Norway, 2011). The DTM image is provided by the Norwegian Mapping Authority via geonorge portal (https://www.geonorge.no/).

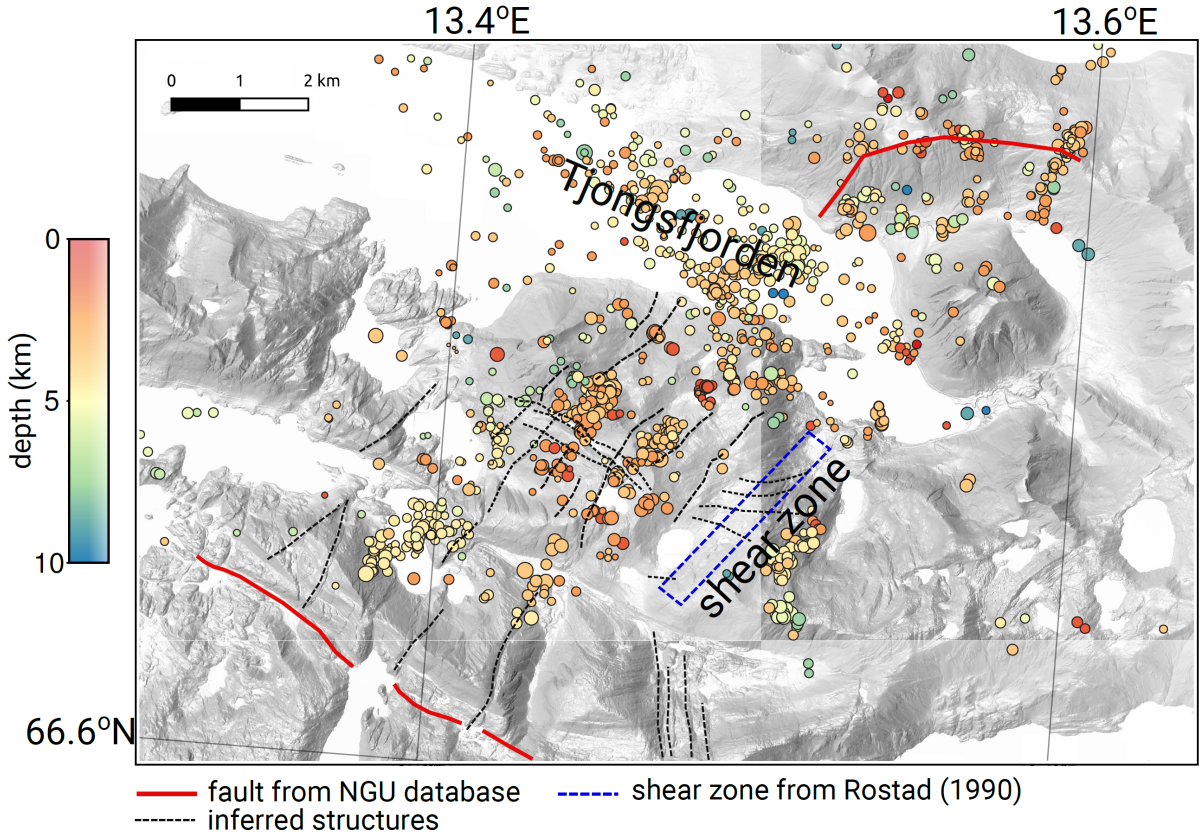

Figure S5. Digital terrain model (DTM) for Jektvik area derived, along with seismicity colored with depth and interpreted structures. The DTM image is provided by the Norwegian Mapping Authority via geonorge portal (https://www.geonorge.no/).

References

Geological Survey of Norway, 2011. Nasjonal berggrunnsdatabase.

Rostad, H., 1990. Strømdal Tunnel Sør: Ingeior Geologisk Rapport (In Norwegian).